Applied Environmental Research (2026) 48(2), 009
https://doi.org/10.35762/AER.2026009

Applied Environmental Research
- RESEARCH FOR SUSTAINABLE PLANET -

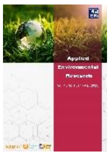

Research Article

Effect of Chromium Doping on The UV- and Sunlight-Driven Photocatalytic Performance of $SrTiO_3$

Ro'ikhatul Jannah[1], Dianisa Khoirum Sandi[2], Fahru Nurosyid[1], Risa Suryana[1], Didier Fasquelle[3], Yofentina Iriani[1,*]

[1] *Department of Physics, Faculty of Mathematics and Sciences, Universitas Sebelas Maret, Jl. Ir. Sutami 36 A Kentingan Surakarta 57126, Indonesia*
[2] *Study Program of Energy Conversion Engineering, Mechanical Engineering, Politeknik Negeri Semarang, Semarang, Indonesia*
[3] *Unit of Dynamic and Structure of Molecular Materials, University of Littoral Côte d'Opale, Calais, France*

*Corresponding Email: yofent_iriani@staff.uns.ac.id

Abstract

Chromium (Cr)-doped strontium titanate ($SrTiO_3$, STO) photocatalysts with compositions of $SrTi1\text{-}xCrxO_3$ (x = 0, 5, and 10%) were prepared via the coprecipitation method. This study aimed to investigate the effects of Cr doping on structural, morphological, and optical properties. Furthermore, this work aimed to examine the photocatalytic performance of pure and Cr-doped STO against methylene blue (MB) degradation under ultraviolet (UV) and sunlight exposure. X-ray diffraction confirmed the formation of the cubic STO phase and the insertion of the Cr dopant in the STO structures. Furthermore, Cr doping reduced the lattice constant, crystallite size, and average particle size and narrowed the band gap from 3.2 (STO) to 2.9 eV (STO:Cr10%). Photocatalytic evaluation via methylene blue degradation revealed contrasting behaviors under different irradiation sources. Under UV irradiation, STO:Cr10% exhibited the highest degradation efficiency (57.23%), whereas under natural sunlight, pure STO showed superior activity (97.15%) compared with Cr-doped samples. These findings indicate that while Cr doping enhances UV-driven photocatalytic activity by modifying the structure and morphology characteristics and narrowing the band gap, pure STO performs more efficiently under sunlight irradiation, possibly because of the absence of dopant-induced recombination centers.

ARTICLE HISTORY

Received: 29 Aug. 2025
Revised: 4 Feb. 2026
Accepted: 10 Feb. 2026
Published: 20 Feb. 2026

KEYWORDS

Strontium titanate;
Chromium doping;
Coprecipitation;
Photocatalyst;
Methylene blue dye;
Photodegradation

Introduction

Owing to their remarkable features and broad applications in sensors, solar cells, fuel cells, energy storage tools, memory devices, and photocatalysis, perovskite-based materials have become a massive concern for researchers worldwide (DuBose and Kamat, 2022; Huang et al., 2024; Sharma et al., 2024). The materials construct the ABO_3 perovskite structure, where the A-sites and B-sites are 12-fold coordinated and 6-fold coordinated cations, respectively, and the O-sites are the oxygen located in the face center of the unit cell (Irshad et al., 2022; Nkwachukwu and Arotiba, 2021). Owing to their stable crystal structure, adjustable bandgap, and thermal and photochemical stability, perovskite oxides have been extensively used as photocatalyst materials in photocatalysis applications (DuBose and Kamat, 2022; Nkwachukwu and Arotiba, 2021; Nkwachukwu et al., 2023). Photocatalyst-based perovskites play a significant role in the photocatalytic process, as they assist in light absorption, electron–hole generation, and redox reactions and further facilitate the degradation of organic pollutants, water splitting, CO_2 reduction, and hydrogen evolution (Irshad et al., 2022; Jagadeeswararao et al., 2023; Jiang et al., 2020; Ordoñez et al., 2024).

Strontium titanate ($SrTiO_3$ or STO) is among many perovskite-structured semiconductors with a cubic structure and has been extensively investigated for its high potential in photocatalytic processes (Chen et al., 2022; Ordoñez et al., 2024). STO has been reported to be an effective photocatalyst material for dye degradation, water splitting, CO_2 reduction, etc. (Elkodous et al., 2023; Kaiya et al., 2024). However, its wide bandgap (3.2 eV) results in poor visible-light absorption and high insulating nature, limiting its photocatalytic performance (Hussain et al., 2020; Kafeshani et al., 2022; Nakamoto et al., 2023). To overcome this drawback, metal doping has been employed to tailor the structural and electronic properties of STO, leading to a reduced bandgap, improved charge separation, and enhanced surface activity. Previous studies have explored various dopants, such as Al (Abdikarimova et al., 2024; Iriani et al., 2024a), Mn (Iriani et al., 2022; 2023), La (Lestari et al., 2025), Fe (Ardi et al., 2024), Mg (Nakamoto et al., 2023), Ni (Kafeshani et al., 2022), La (Iriani et al., 2024) , V (Xu et al., 2025), and Cr (Lopez-Juarez 2025; Qin et al., 2024; Wang et al., 2006), in STO, all of which have demonstrated improved photocatalytic efficiency.

Although extensive studies have reported metal-doped STO photocatalysts, investigations focusing on chromium (Cr)-doped STO remain relatively scarce, particularly in the context of dye degradation under different irradiation sources. Previous studies on Cr-doped STO have focused primarily on visible-light activation or water-splitting performance, whereas systematic comparisons between UV and natural sunlight irradiation are rarely discussed. Moreover, the dual role of Cr dopants as bandgap modifiers and potential recombination centers has not been sufficiently clarified.

In this work, Cr doping levels of 5% and 10% were selected to represent moderate and relatively high substitution regimes at the Ti site, where defect formation and electronic structure modification are expected to be significant. By directly comparing the photocatalytic activity under UV and sunlight irradiation, this study reveals an activity inversion phenomenon, providing insight into how dopant-induced defect states influence the charge carrier dynamics under different spectral conditions. This approach offers a more nuanced understanding of dopant–light-source interactions in perovskite photocatalysts than conventional bandgap narrowing methods.

To clearly position the present work within existing studies, Table 1 summarizes representative reports on Cr-doped $SrTiO_3$ photocatalysts for dye degradation under various irradiation conditions. Compared with previous studies, this work uniquely demonstrates a clear inversion in photocatalytic performance between UV and natural sunlight irradiation for Cr-doped $SrTiO_3$. While most earlier reports focused on visible-light activation or water-splitting reactions, this study highlights the critical interplay between dopant-induced defect states and the irradiation spectrum, providing insight into why bandgap narrowing alone does not guarantee improved solar-driven photocatalysis.

Additionally, recent studies employing sludge-derived magnetic photocatalysts, TiO_2- and Fe_3O_4-based composites, and biophotocatalytic systems have demonstrated that dye degradation performance is governed by a combination of light absorption, surface adsorption, and radical-mediated oxidation pathways rather than bandgap engineering alone (Rastgar et al., 2022; 2023; 2024; 2025; Zamani et al., 2023a; b). These findings highlight the importance of carefully interpreting the photocatalytic results obtained using dye model pollutants.

Materials and methods

1) Materials

The raw materials included strontium nitrate ($Sr(NO_3)_2$), titanium tetra butoxide ($Ti(C_4H_9O)_4$), and chromium(III) nitrate nonahydrate ($Cr(NO_3)_3{\cdot}9H_2O$) as the sources of Sr, Ti, and Cr, respectively. Other materials used were oxalic acid ($C_2H_2O_4$) and isopropyl alcohol ($(CH_3)_2CHOH$). All chemical reagents used in this study were of analytical grade and were used without further purification.

2) Synthesis of pure and Cr-doped STO

Pure and Cr-doped STO, with the formula $SrTi_{1-x}Cr_xO_3$ (x = 0, 5, and 10%), was synthesized via the coprecipitation method. For pure STO, oxalic acid and isopropyl alcohol were initially mixed by stirring for 20 minutes at a speed of 250 rpm. Moreover, titanium tetrabutoxide was separately mixed with isopropyl alcohol via the same method. The solution was then added to the oxalic solution and continuously stirred, and strontium nitrate was added after 20 min. Afterwards, the solution was titrated for 1 hour with distilled water, after which it was allowed to precipitate for 24 hours. The sample was washed simultaneously with ethanol and distilled water and then dried at 100 °C for 10 hours. The powdered sample was crushed and sintered at 900 °C. Finally, the powder sample was reground to obtain more homogeneous particles and was ready to be characterized.

For the Cr-doped STO ($SrTi_{0.95}Cr_{0.05}O_3$ and $SrTi_{0.90}Cr_{0.10}O_3$), the procedures used were the same. However, in this process, chromium(III) nitrate nonahydrate was added immediately after the titanium tetrabutoxide and oxalic acid solutions were added. All samples were labeled STO, STO:Cr5%, and STO:Cr10%, corresponding to Cr dopant concentrations of 0%, 5%, and 10%, respectively.

Table 1 Comparative results of Cr-doped STO studies

Study	Synthesis method	Cr content	Bandgap (eV)	Light source	Target pollutant/ reaction	Main findings
Wang et al. (2006)	Solid-state	0.5–5 at.%	~2.7–3.0	Visible	Water splitting	Cr introduces mid-gap states; high Cr increases recombination
Lopez-Juarez (2021)	Microwave-hydrothermal	1–5 mol%	~2.8	UV–Vis	RhB degradation	Improved visible-light response but stability not discussed
Jiang et al. (2020)	Hydrothermal	1–3 at.%	~2.6	Visible	H_2 evolution	Enhanced absorption; performance sensitive to Cr level
Qin et al. (2024)	Solid-state reaction	0.5–3 at.%	~2.7	Visible	Overall water splitting	Defect–charge delocalization critical for activity
Ichihara et al. (2019)	Sol–gel	1–10 at.%	~2.6–3.0	UV–Vis	Charge carrier dynamics	High Cr accelerates recombination (TAS evidence)
This work	Coprecipitation	5 & 10%	3.20 → 2.90	UV & Sunlight	MB degradation	Activity inversion: Cr enhances UV activity but suppresses sunlight performance due to recombination effects

3) Characterization

The prepared samples were characterized via various techniques and instruments. X-ray diffraction (XRD) (Bruker D8 Advanced with a Cu source Kα of 1.5406 Å) was performed to determine the structural properties. Fourier transform infrared spectroscopy (FTIR) (Shimadzu A21004802518) was used to examine the functional groups of the samples. FTIR spectra were recorded in transmittance mode over the wavenumber range of 350–4,000 cm^{-1}. Scanning electron microscopy (SEM) with energy dispersive X-ray (EDX) analysis (Quanta 250/450/650) was used to observe the morphological features and elemental compositions of the samples. UV–Vis diffuse reflectance spectroscopy (UV–Vis DRS) (Lambda 365+ from PerkinElmer) was used to examine the optical properties of the samples over a wavelength range of 200–700 nm.

4) Photocatalytic performance evaluation

The photocatalytic performance of the prepared pure and Cr-doped STO was evaluated through the photodegradation of methylene blue under a 25-watt UV lamp and direct sunlight exposure. First, 0.05 g of the prepared samples were dissolved in 50 mL of 10 ppm MB solution.

The first photodegradation experiment was conducted in a dark room for 30 minutes to establish adsorption equilibrium. For UV irradiation, the solution was kept in a dark room and irradiated with a UV lamp. Five milliliters of irradiated solution was collected every 60 minutes for a total duration of 240 minutes. Moreover, for sunlight irradiation, the equilibrium solution was exposed to direct sunlight, and 5 mL of each exposed solution was collected every 30 minutes for a total duration of 180 minutes. Both UV-irradiated and sunlight-irradiated samples were then centrifuged and tested via a UV–Vis spectrophotometer (HITACHI UH530) to investigate the absorbance profiles in the wavelength range of 400–800 nm.

The absorbance data were then exploited to estimate the % degradation of methylene blue through Eq.1. where C_0 and C_t are the initial concentration (before UV irradiation) and the concentration after t UV irradiation, respectively. The photodegradation kinetics were also determined via Equation 2. By plotting $\mathbf{ln(A_0/A_t)}$ vs. t, the kinetic rate of photodegradation (k) by each prepared photocatalyst sample can be determined from the slope of the graph (Sandi et al., 2025).

$$\%\mathrm{MB\ degradation} = [(A_0 - A_t)/A_0] \times 100\% \quad \text{(Eq.1)}$$

$$\ln(C_0/C_t) = kt \quad \text{(Eq.2)}$$

Results and discussion

1) Structural property

Figure 1(a) shows the XRD patterns of the pure and Cr-doped STO samples. All peaks were identified with the International Center for Diffraction Data (ICDD) and agreed with database number 201257 from ICDD#84--0444. The peaks were confirmed to belong to the cubic STO phase with space group Pm3m and planes (100), (110), (111), (200), (210), (211), and (220). The symbols (*) in the XRD patterns of STO and STO:Cr5% denote the impurities $SrCO_3$ and TiO_2 resulting from the synthesis process. Nevertheless, there was no significant change in the peak position of the Cr-doped samples. Nevertheless, slight right shifts were detected in the doped samples (Figure 1(b)), indicating that the doping had been appropriately performed. This shift indicates a modification in the crystal lattice induced by Cr doping, as presented in Figure 1(c) (Xu et al., 2025).

Figure 1(c) displays the lattice strains and crystallite sizes of the pure and Cr-doped STO samples obtained with the Debye–Scherrer formula (Tsaviv et al., 2024). The crystallite size of the prepared samples clearly decreases with increasing Cr dopant concentration. Doping Cr in STO can inhibit crystal growth during the synthesis process due to lattice distortion caused by Cr insertion in the Ti sites in the STO lattice (Chen et al., 2018; Khoudro et al., 2024). This is also evident from the increase in lattice strain due to doping, as shown in Figure 1(c). The difference in the atomic size of the donor (Cr) and receptor (Ti) induces internal strain, leading to increased lattice strain and reduced crystallite size (Khoudro et al., 2024; Stajcic et al., 2024).

The XRD data were then processed via the Rietveld refinement method via GSAS software, and the results are shown in Table 2. The results confirm that all the prepared samples exhibit a cubic structure. The goodness of fit (GOF), x^2, and R values represent the quality of the experimental data fitting. The results demonstrate that the values of these parameters were relatively low, indicating that the refinement process was reliable. Additionally, the values decreased with increasing amounts of the Cr dopant, suggesting that doping influences the STO structure due to differences in ionic radii, whereas the cubic crystal structure remains unchanged. Table 1 also presents the lattice constants of the prepared samples obtained from this analysis, showing that the values decrease with increasing Cr dopant concentration, which is consistent with the Debye–Scherrer estimation.

The 3D visualization of the crystal structure of pure and Cr-doped $SrTiO_3$ (STO) was modeled and visualized via VESTA software, as shown in Figures 1(d) and 1(e). Both structures are represented as 2×2×2 supercells to clearly illustrate the lattice configuration. Figure 1(d) shows the perovskite structure of pure STO, which consists of Sr atoms occupying the corners of a cubic unit cell, Ti atoms positioned at body centers, and O atoms located at face centers. This arrangement corresponds to the typical ABO_3 perovskite structure, with Sr acting as the A-site cation, Ti acting as the B-site cation, and O acting as the anion.

Moreover, Figure 1(e) depicts Cr-doped STO (STO: Cr10%), in which Ti atoms are partially substituted by Cr atoms at the B-site positions of the perovskite lattice. The incorporation of Cr dopants into the Ti sites demonstrated that the doping process was successfully achieved without disrupting the overall cubic perovskite framework. Thus, this visualization confirms the structural feasibility of incorporating Cr into the STO lattice.

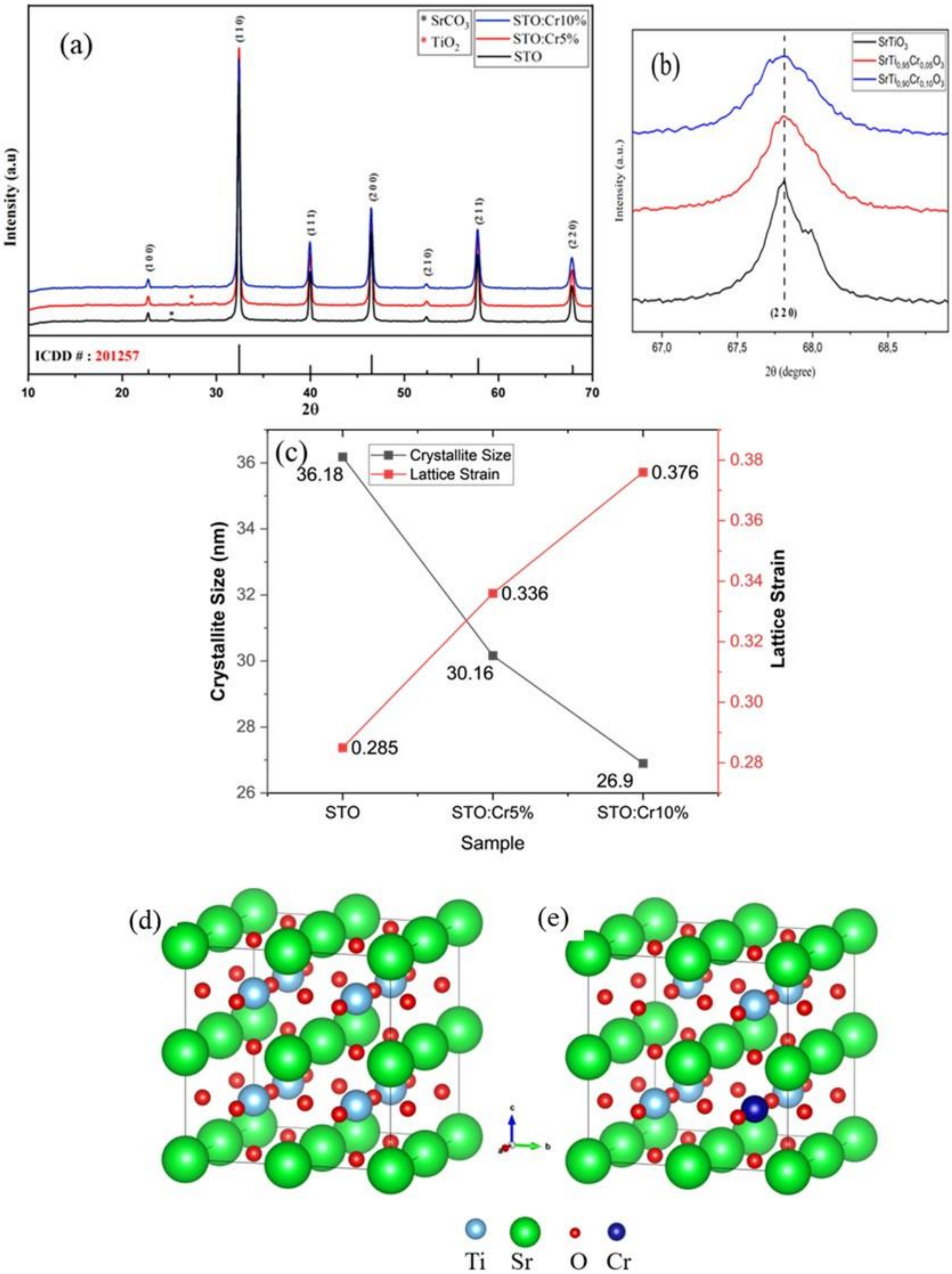

Figure 1 (a) XRD patterns of pure and Cr-doped STO samples, (b) right peak shift at Cr-doped STO in comparison with pure STO, (c) crystalline size and lattice strain (ε) of pure and Cr-doped STO, (d) illustration of 3D visualization of the crystal structure of STO, and (e) illustration of 3D visualization of the crystal structure of STO:Cr10%

Table 2 The results of Rietveld refinement via the GSAS software

Sample	a=b=c (Å)	x^2	Rw (%)	GOF
STO	3.91231	1.842	7.147	1.36
STO:Cr5%	3.90781	1.420	6.255	1.19
STO:Cr10%	3.90712	1.356	6.180	1.16

2) Functional group

Figure 2 shows the FTIR spectra of the pure and Cr-doped STO samples. The broad peaks at 3,096 cm^{-1}–3,456 $cm^{-1}$and 3,550 cm^{-1}–3,650 cm^{-1} denoted the presence of O–H stretching from surface hydroxyls/ adsorbed moisture (Asefa et al., 2024; Murthy et al., 2024). The weak peak at 2910 cm^{-1} represented the vibration of the C–H stretching of residual organics from the synthesis process (Asefa et al., 2024; Iriani et al., 2022). The band at approximately 1700–1500 cm^{-1} (labeled COOH/N–H in the figure) can be attributed to the C=O stretching of carboxyl/carbonate-type surface species and/or N–H bending from residual precursors. The bands at approximately 900–1,000 cm^{-1} corresponded to the typical perovskite lattice vibrations of Ti–O. In addition, the intense peaks at 500–800 cm^{-1} were associated with Sr–Ti–O (TiO_6 octahedral) stretching/bending modes that are characteristic of the $SrTiO_3$ framework (Iriani et al. 2024b; Lopez-Juarez, 2021). The presence of these forms corresponds to the successful formation of pure and Cr-doped STO, which is consistent with the XRD data.

Furthermore, Cr^{3+} ions replacing Ti^{4+} in the STO lattice slightly affected the positions and transmittance intensity of the existing bonds, especially the Sr–Ti–O bonds. The Cr doping slightly changed the wavelength positions of the Sr–Ti–O bonds from 571.918 cm^{-1} ($SrTiO_3$) to 576.740 cm^{-1} (STO:Cr5%) and 584.456 cm^{-1} (STO: Cr10%). In addition, it also reduced the transmittance intensity from 36.637 (SrTiO3) to 22.688 (STO:Cr5%) to 11.426 (STO:Cr10%). The insertion of Cr^{3+} ions into the STO lattice can create new absorption centers, thereby increasing the material's interaction with infrared light (Chen et al., 2018; Hasan et al., 2022). Overall, the spectral changes validate the successful incorporation of Cr into the perovskite lattice and its impact on the vibrational structure of STO.

3) Morphological properties

Morphological images of pure and Cr-doped STO are depicted in Figure 3. All the samples exhibited irregular particle shapes with several agglomerations, a characteristic typical of nanoparticles synthesized via wet chemical techniques. The particle size distributions obtained from Gaussian fitting are presented along with the SEM images. For pristine STO (Figure 3(a)), the particle size distribution is centered at ~156 nm, with most particles ranging from 120–200 nm. After Cr incorporation, the average particle size decreases significantly to ~117 nm for STO:Cr5% (Figure 3 (b)) and ~107 nm for STO:Cr10% (Figure 3(c)), with narrower distributions than those of the undoped sample.

The reduction in particle size with increasing Cr content indicates that doping influences the nucleation and growth dynamics during synthesis. Specifically, the presence of Cr dopants enhances the nucleation rate while suppressing particle growth, resulting in smaller final particle sizes (Flores et al., 2024; Huo et al., 2018). This effect results in more uniform distributions with reduced average diameters as the doping level increases.

Table 3 summarizes the average particle size and R^2 values obtained from Gaussian fitting. The high R^2 values (0.98–0.99) confirm the reliability of the fitting results. Furthermore, the observed trend of particle size from the reduction is consistent with the crystallite size calculated XRD analysis. These findings support the conclusion that Cr doping not only alters the structural properties but also refines the morphology of STO particles.

Figure 4 presents the results of the EDX analysis, which show the presence of Sr, Ti, Cr, and C in the Cr-doped samples. The appearance of the carbon element is due to contamination during sample preparation for the SEM-EDX test. This contamination is characteristically associated with the use of carbon-based adhesive tape or glue to mount the samples on the sample holder.

Furthermore, the results revealed the presence of Cr, indicating that the doping was successful. Table 4 shows the mass and atomic percentage of each element in the samples. The mass and atomic percentage of Cr slightly increased from the STO:Cr5% to the STO:Cr10% samples, corresponding to the doping quantity. In contrast, the percentage of Ti slightly decreases because its position is partially replaced by Cr in the STO lattice. These results were as expected and consistent with the designed doping ratio. Overall, these EDX findings validate the successful incorporation of Cr into the STO lattice and support the previously proposed structural model, which is consistent with the XRD and FTIR analyses.

Table 3 Average particle size and R-square value

Sample	Average particle size (nm)	R-square (R^2)
STO	155.82 ± 0.58	0.98
STO:Cr5%	116.95 ± 0.87	0.98
STO:Cr10%	106.75 ± 0.39	0.99

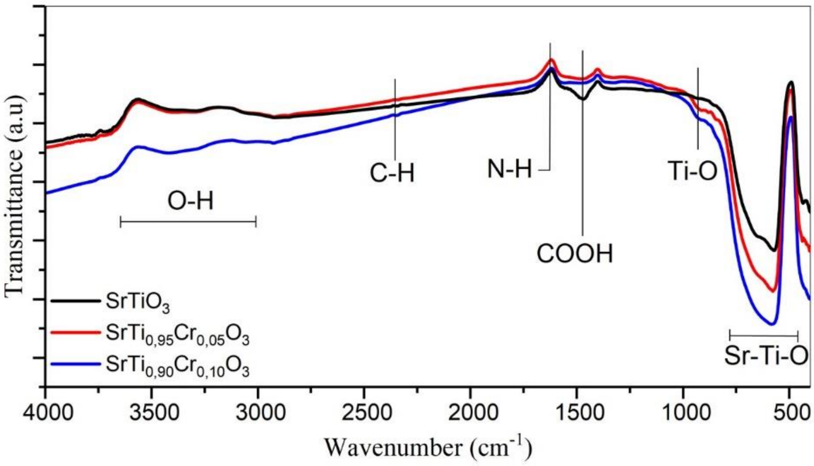

Figure 2 FTIR spectra of pure and Cr-doped STO.

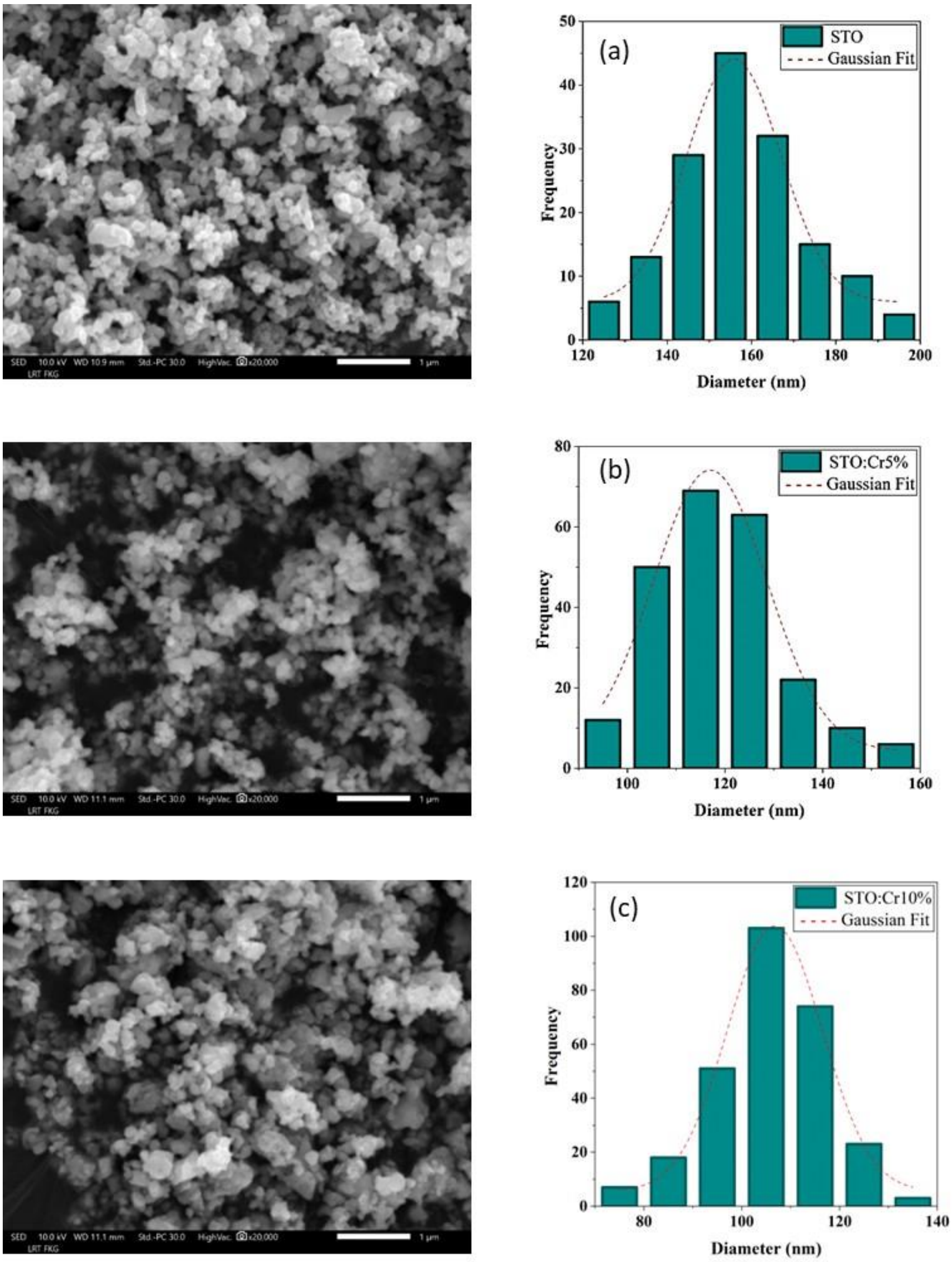

Figure 3 Morphological images and particle size distributions of (a) STO, (b) STO:Cr5%, and (c) STO:Cr10%.

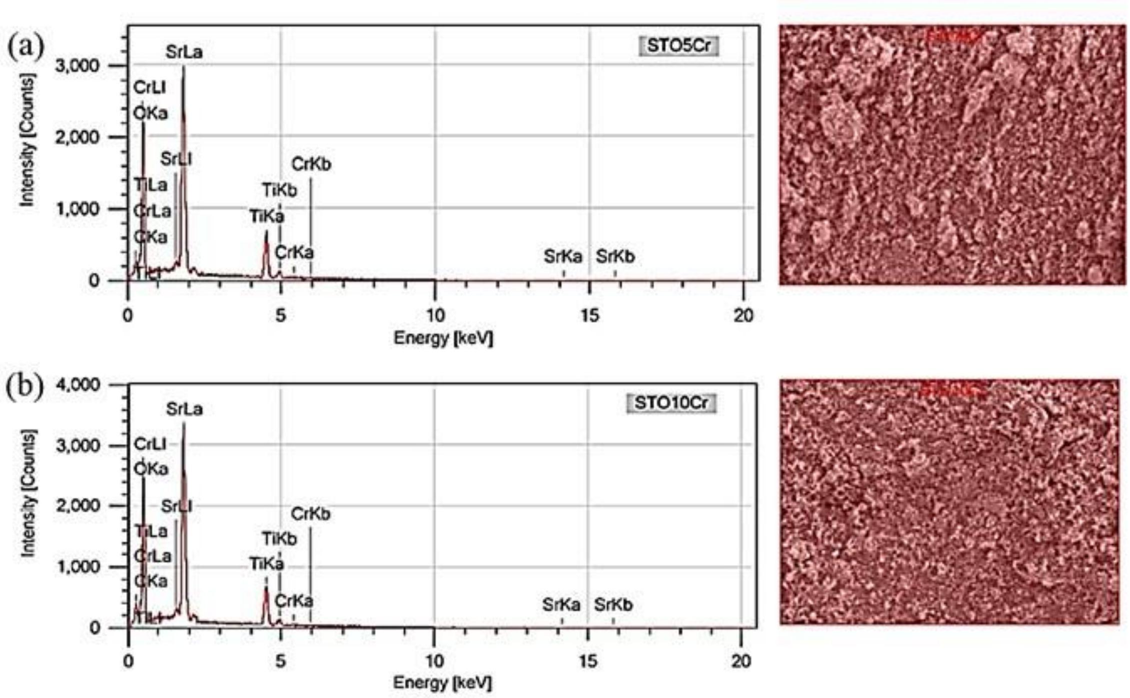

Figure 4 EDX results of (a) STO:Cr5% and (b) STO:Cr10%.

Table 4 Mass and atomic percentage of the elements in the Cr-doped samples

Element	Mass (%)		Atoms (%)	
	STO:Cr5%	STO:Cr10%	STO:Cr5%	STO:Cr10%
C	3.20 ± 0.05	4.43 ± 0.06	9.74 ± 0.16	13.10 ± 0.17
O	21.23 ± 0.20	21.12 ± 0.19	48.54 ± 0.46	46.88 ±0.42
Ti	28.44 ± 0.45	28.36 ± 0.43	21.73 ± 0.35	21.03 ±0.32
Cr	1.07 ± 0.17	1.12 ± 0.42	0.75 ± 0.12	0.76 ± 0.11
Sr	46.06 ± 0.44	44.97 ± 0.42	19.23 ± 0.19	18.23 ± 0.17

4) Optical properties

Figure 5 shows the reflectance curves of the pure and Cr-doped STO samples, along with the corresponding Tauc plots presented in the inset. The graph shows significant reflectance peaks at wavelengths of approximately 360 nm and 700 nm, where the area approximately 360 nm corresponds to the region of bandgap transition. This region underwent a slight redshift due to Cr doping, indicating a modification of the bandgap energy. Furthermore, the reflectance significantly decreased in the Cr-doped samples. The decreased reflectance intensity of the Cr-doped samples indicates enhanced light absorption due to the incorporation of Cr into the perovskite lattice. This further creates new energy levels in the energy band gap and reduces the reflectance (Ikram et al., 2023; Miran et al., 2023; Xu et al., 2025).

In terms of optical properties, the estimation of the bandgap energy is crucial. The optical bandgap values were determined via the Kubelka–Munk function and Tauc plot method by extrapolating the linear portion of the $(\alpha h\nu)^2$ versus hν curve to the energy axis (inset of Figure 6). The estimated bandgap values were 3.20, 3.00, and 2.90 eV for SrTiO3, STO:Cr5%, and STO:Cr10%, respectively. The results indicate that the pure STO obtained in this study has a bandgap of 3.20 eV, which is consistent with the theoretical value reported in the literature. Furthermore, Cr doping could effectively narrow the bandgap values from 3.00 eV (STO:Cr5%) to 2.90 eV (STO:Cr10%). This reduction is attributed to the changes in the crystallites and particle sizes of the samples, which are influenced by Cr doping. The reduced crystallite and particle sizes due to Cr doping can induce a narrowed band gap in the samples (Iriani et al., 2024b; Talanov et al., 2024).

5) Photocatalytic performance

The photocatalytic performance of Cr-doped STO was successfully assessed. However, it should be noted at the outset that the present study focused on correlating structural, morphological, optical, and photocatalytic performance data. Direct experimental evaluation of charge carrier dynamics, such as recombination rates, trap-state distributions, and charge transfer resistance, was not conducted because of the absence of transient absorption spectroscopy (TAS), photoluminescence (PL), and X-ray photoelectron spectroscopy (XPS) measurements. Therefore, discussions related to charge transport and recombination behavior are based on indirect evidence and supported by previously reported studies on Cr-doped $SrTiO_3$ systems.

Figure 6 shows the UV–Vis absorbance spectra of MB solutions irradiated with UV light and sunlight in the presence of pure STO and Cr-doped STO photocatalysts. The inset photographs display the corresponding color changes of the MB solutions at various irradiation times. Under UV irradiation, no substantial visual color change was observed; nevertheless, the absorbance intensity at ~664 nm decreased progressively over the irradiation period from 0--240 minutes. In contrast, under sunlight irradiation, noticeable fading of the MB solution was observed, which was consistent with a decrease in absorbance over the 0–180-minute period. These findings indicate that the photocatalytic degradation efficiency increases with irradiation time, with a more pronounced effect under solar exposure.

The degradation efficiencies after 240 minutes of UV irradiation and 180 minutes of sunlight irradiation are summarized in Table 4. Under UV irradiation, STO: Cr10% exhibited the highest degradation efficiency, followed by pure STO, while STO:Cr5% showed the lowest activity. In contrast, under sunlight irradiation, pure STO achieved the highest degradation performance, followed by STO:Cr10% (78.71%) and STO:Cr5% (65.20%). These results confirm that the photocatalytic activity of STO is strongly influenced by both the dopant concentration and the type of light source.

Although Cr doping reduces the crystallite size and particle size and narrows the bandgap, higher doping levels may also introduce defect states and the possibility of nonuniform dopant distributions, which act as recombination centers, thus reducing the number of effective charge carriers (Ichihara et al., 2019; Sharma et al., 2024). In addition, sunlight, with its broader spectrum and higher photon flux, is sufficient to activate pure STO without giving a chance for recombination, making it more efficient for solar-driven photocatalysis (Galloni et al., 2022; Navalon et al., 2023; Okunaka et al., 2024). These results indicate that the effect of Cr doping is highly dependent on the irradiation source. While Cr doping increases the photocatalytic activity under UV light, pure STO remains superior under sunlight because of its stable band structure and lower charge recombination (Namade et al., 2025; Tenzin et al., 2021).

The photocatalytic behavior of Cr-doped $SrTiO_3$ can be rationalized by considering the dual role of Cr^{3+} dopants in modifying the electronic structure. Substitution of Ti^{4+} by Cr^{3+} introduces localized 3d-derived mid-gap states above the valence band of $SrTiO_3$, which effectively extend light absorption toward lower photon energies and facilitate charge carrier excitation under UV irradiation (Ichihara et al., 2019; Wang et al., 2006). Similar Cr-induced defect states in $SrTiO_3$ have been reported to enhance photocatalytic activity by promoting charge separation at moderate dopant concentrations (Lopez-Juarez, 2021; Qin et al., 2024).

However, excessive Cr incorporation can lead to an increased density of defect states that act as recombination centers, accelerating electron–hole recombination and reducing the availability of reactive charge carriers for surface redox reactions (Ichihara et al., 2019; Wang et al., 2006). Transient absorption spectroscopy studies on Cr-doped $SrTiO_3$ have confirmed that higher Cr concentrations significantly shorten charge carrier lifetimes due to enhanced recombination via Cr-related trap states (Ichihara et al., 2019). These findings provide a mechanistic basis for the concentration-dependent photocatalytic trends observed in this study.

Table 5 Degradation levels after 240 min (UV) and 180 min (sunlight) of irradiation

Sample	% Degradation	
	UV	Sun
STO	48.79%	97.15%
STO:Cr5%	29.58%	65.20%
STO:Cr10%	57.23%	78.71%

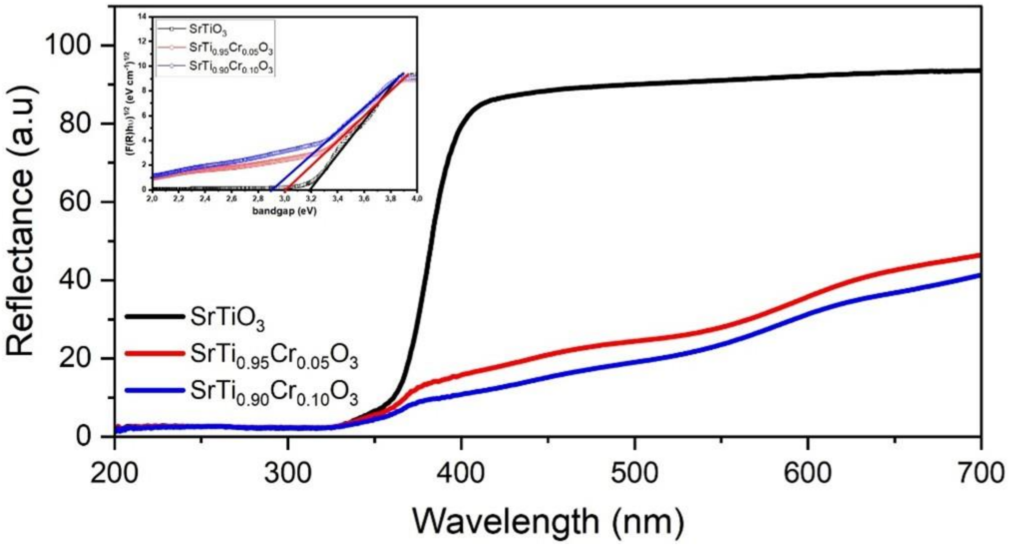

Figure 5 Reflectance curves and Tauc plot (inset picture) of pure and Cr-doped STO.

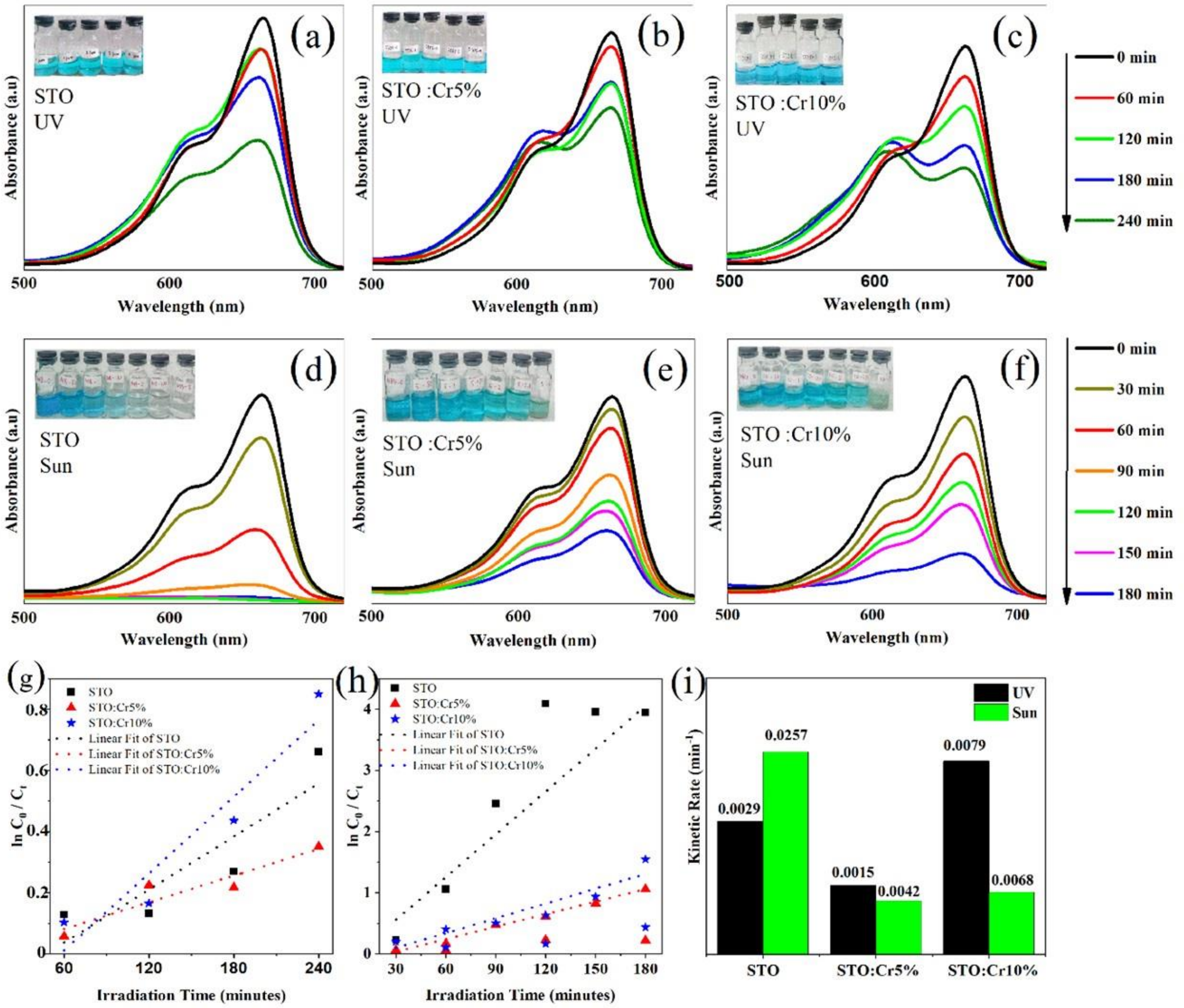

Figure 6 (a-c) UV–Vis spectra of UV-irradiated MB solutions with various irradiation times, (d-f) UV–Vis spectra of sunlight-irradiated MB solutions with various irradiation times, (g-h) photodegradation kinetics of pure and Cr-doped STO samples under UV and sunlight irradiation, and (i) kinetic rates.

Under UV irradiation, both pristine and Cr-doped $SrTO_3$ generate electron–hole pairs that participate in surface redox reactions, leading to the formation of reactive oxygen species (ROS), such as hydroxyl radicals (•OH) and superoxide radicals ($•O_2^-$). Similar ROS-dominated degradation pathways have been widely reported in TiO_2^-, $Fe_3O_4^-$, and sludge-derived photocatalytic systems applied for dye and wastewater treatment under UV or UVA irradiation (Rastgar et al., 2023; 2024; 2025; Zamani et al., 2023a). In this context, Cr doping enhances UV-driven photocatalytic activity by improving photon absorption and charge generation efficiency, particularly at lower dopant levels.

In contrast, under broadband sunlight irradiation, pristine $SrTO_3$ has superior photocatalytic performance compared with that of Cr-doped samples. Owing to its broader spectral distribution and higher photon flux, sunlight is sufficient to activate pure $SrTO_3$ efficiently without introducing significant recombination losses, making it more effective for solar-driven photocatalysis (Galloni et al., 2022; Okunaka et al., 2024; Navalon et al., 2023). The stable intrinsic band structure of undoped $SrTO_3$ minimized defect-induced recombination, allowing more effective utilization of photogenerated charge carriers under solar irradiation (Namade et al., 2025; Tenzin et al., 2021).

In addition to intrinsic charge carrier processes, the role of methylene blue as a photosensitizer should also be considered, particularly under sunlight irradiation. Previous studies on low-cost magnetic char, sludge-derived photocatalysts, and biobased systems have shown that the MB degradation efficiency is strongly influenced by the adsorption behavior and dye–surface interactions prior to photocatalytic oxidation (Rastgar et al., 2022; 2023; Zamani et al., 2023b). These findings suggest that the observed photocatalytic activity under sunlight irradiation may involve dye photosensitization mechanisms, where excited MB molecules can inject electrons into the conduction band of the photocatalyst, contributing to ROS formation and apparent degradation efficiency (Galloni et al., 2022; Nkwachukwu et al., 2023).

Accordingly, in the present study, the superior sunlight-driven performance of pristine $SrTO_3$ over Cr-doped samples is interpreted not only as a consequence of band structure effects but also as the result of the combined influence of surface properties, defect density, and potential suppression of dye-sensitized pathways by dopant-induced recombination centers.

Therefore, the observed inversion in photocatalytic activity under UV and sunlight irradiation reflects a balance between dopant-induced absorption enhancement and recombination losses rather than bandgap narrowing alone. These results clearly indicate that the effect of Cr doping on $SrTO_3$ is highly dependent on the irradiation source, with Cr-induced defect states enhancing UV-driven photocatalysis but potentially hindering performance under broadband solar illumination.

Furthermore, the structural stability of the catalysts is supported by the preservation of the cubic perovskite phase after Cr incorporation, as confirmed by XRD and Rietveld refinement. However, cyclic stability and reusability tests were not performed in this study and should be addressed in future work to evaluate long-term photocatalytic durability.

Overall, this study demonstrated that chromium doping effectively modifies the structural and optical properties of $SrTO_3$; however, its influence on photocatalytic performance strongly depends on the irradiation source. While Cr-induced defect states enhance UV-driven photocatalytic activity, they may also promote charge carrier recombination under broadband sunlight irradiation. The observed activity inversion highlights that bandgap narrowing alone is insufficient to predict solar photocatalytic performance, emphasizing the need to balance the dopant concentration with the spectral characteristics of the light source.

These findings imply that the role of dopant-induced defect states and irradiation-dependent photocatalytic behavior observed in Cr-doped $SrTO_3$ may offer broader insight into defect engineering strategies in perovskite-type oxides. Similar approaches could be extended to other perovskite-based photocatalysts, such as $BaTiO_3$, $CaTiO_3$, and $LaFeO_3$, where controlled dopant incorporation may be used to tune light absorption and charge carrier behavior. However, such extensions require independent experimental validation and should not be directly extrapolated from the present results.

The contrasting photocatalytic trends observed under UV and sunlight irradiation further indicate that the dopant design must be carefully optimized with respect to the intended light source and operating conditions. While dopant-induced defect states can be beneficial for UV-driven photocatalysis by enhancing photon absorption and charge generation, they may simultaneously promote recombination losses under broadband solar irradiation. This observation underscores that bandgap narrowing alone is insufficient as a universal design criterion for solar photocatalysts.

Nevertheless, this study was limited by relatively low Cr doping concentrations (up to 10%) and focused primarily on microstructural and optical correlations with photocatalytic activity. The electronic band structure and charge carrier dynamics were not experimentally analyzed via advanced spectroscopy methods such as PL, XPS, or EIS. Furthermore, only methylene blue dye was used as a model pollutant; thus, broader pollutant categories should be examined for general applicability.

Hence, future work should explore a wider range of dopant concentrations, codoping strategies, and computational modeling to achieve a deeper understanding of defect formation, electronic transitions, and charge carrier behavior in $SrTO_3$-based systems. In particular, the combination of Cr with other dopants (e.g., La, Fe, or Ni) could reveal synergistic effects for visible-light-driven photocatalysis. Additionally, long-term stability tests and reusability assessments are crucial for evaluating the practical feasibility of Cr-doped $SrTO_3$ in real wastewater treatment applications.

Conclusions

Pure and Cr-doped $SrTO_3$ photocatalysts were successfully synthesized via the coprecipitation method, and the effects of Cr doping at 5% and 10% were investigated. Structural and elemental analyses confirmed successful Cr incorporation into the STO lattice, leading to reduced crystallite size, particle size, and bandgap energy. Photocatalytic evaluation via methylene blue degradation revealed contrasting behavior depending on the irradiation source. Cr doping enhanced the photocatalytic activity under UV irradiation, with STO: Cr10% exhibiting the highest degradation efficiency, whereas pure STO showed superior performance under sunlight. These results indicate that dopant-induced defect states play a dual role, enhancing UV-driven activity but promoting charge recombination under solar irradiation. This study highlights the importance of optimizing the dopant concentration in relation to the intended light source for photocatalytic environmental remediation applications.

Acknowledgements

The authors thank Universitas Sebelas Maret for supporting this research through RKAT Universitas Sebelas Maret TA 2025, Kolaborasi Internasional (KI-UNS), with contract number 369/UN27.22/PT.01.03/2025.

Data availability statement

Information and data used in the study will be disclosed upon request.

Author ORCID

Ro'ikhatul Jannah: 0009-0003-4134-6665
Dianisa Khoirum Sandi: 0000-0001-9287-3949
Fahru Nurosyid: 0000-0003-3459-2721
Risa Suryana: 0000-0002-8754-6019
Didier Fasquelle: 0000-0002-1947-1860
Yofentina Iriani: 0000-0003-3899-8286

Author contributions

Ro'ikhatul Jannah: Methodology, Investigation, Writing – Original draft, Visualization
Dianisa Khoirum Sandi: Formal analysis, Data curation, Writing – Review &editing, Visualization
Fahru Nurosyid: Validation, Supervision
Risa Suryana: Validation, Supervision
Didier Fasquelle: Conceptualization, Validation, Supervision
Yofentina Iriani: Conceptualization, Validation, Supervision, Project administration, Funding acquisition

Conflicts of interest

The authors declare that there are no conflicts of interest in competing financial or personal relationships that could have appeared to influence the work reported in this work.

References

Abdikarimova, U., Bissenova, M., Matsko N., Issadykov, A., Khromushin, I., Aksenova, T., Munasbayeva, K., Slyamzhonov, E., & Serik, A. (2024). Visible light-driven photocatalysis of Al-doped $SrTiO_3$: experimental and DFT study. *Molecules, 29*(22), 5326.

Ardi, E. K. A., Iriani, Y., & Fasquelle, D. (2024). Ferrite (Fe) doping in strontium titanate ($SrTi_{1-x}Fe_xO_3$) to improve photocatalytic activity. *Advances in Science and Technology, 141*, 71–76.

Asefa, G., Negussa, D., Lemessa, G., Alemu, T., & Sabir, F. K. (2024). The study of photocatalytic degradation kinetics and mechanism of malachite green dye on Ni–TiO_2 surface modified with polyaniline. *Journal of Nanomaterials, 2024*, 1–11.

Chen, Y., Xu, J., Xie, S., Tan, Z., Nie, R., Guan, Z., Wang, Q., & Zhu, J. (2018). Ion doping effects on the lattice distortion and interlayer mismatch of aurivillius-type bismuth titanate compounds. *Materials (Basel), 11*(5), 821.

Chen, X., Qi, H., Zhang, C., Ma, L., Li, Z., Chen, P., Xine, Q., Sun, Q., & Yan, Z. (2022). Synthesis and characterization of recyclable PVA/$SrTiO_3$/Ag_2O composite with photocatalytic degradation performance of methylene blue. *Applied Physics A, 128*(5), 128.

DuBose J. T., & Kamat, P. V. (2022). Efficacy of perovskite photocatalysis: Challenges to overcome. *ACS Energy Letters, 7*(6), 1994–2011.

Elkodous, M. A., El-Khawaga, A. M., Abouelela, M. M., & Maksoud, M. I. A. A. (2023). Cocatalyst loaded Al-$SrTiO_3$ cubes for Congo red dye photo-degradation under wide range of light. *Scientific Reports*, *13* (1), 6331.

Flores, E. M., Barrios, B. S. V., Huillca J. C. H., Garcia, J. A. C., Bravo, C. A. P., Mendoza, H. E. N., Cohaila, A. B. Q., Gomex, F. G., Calderon, R. M. T., Quispe, G. L. F., & Sacari, E. J. S. (2024). Cr^{3+} doping effects on structural, optical, and morphological characteristics of $BaTiO^3$ nanoparticles and their bioactive behavior. *Crystals, 14*(11), 998.

Galloni, M. G., Cerrato, G., Giordana, A., Falletta, E., & Bianchi, C. L. (2022). Sustainable solar light photodegradation of diclofenac by nano- and micro-sized $SrTiO_3$. *Catalysts,* 12(8), 804.

Hasan, T., Saha, A., Khan, M. N. I., Rashid, R., Basith, M. A., Bashar, M. S., & Ahmed, I. (2022). Structural, electrical, and magnetic properties of Ce and Fe doped $SrTiO_3$. *AIP Advances, 12*(9), 095003.

Huang, Y., Yu, J., Wu, Z., Li, B., & Li, M. (2024). All-inorganic lead halide perovskites for photocatalysis: A review. *RSC Advances, 14*(7), 4946–4965.

Huo, J., Li, W., Wang, T. (2019). Effect of Cr doping concentration on the structural, optical, and electrical properties of lead sulfide (PbS) nanofilms. *Coatings, 9*(6), 376.

Hussain, T., Junaid, M., & Qayyum, H. A. (2020). Preparation of Ba-doped $SrTiO_3$ photocatalyst by sol-gel method for hydrogen generation. *Chemical Physics Letters, 754*, 137741.

Ichihara, F., Sieland, F., Pang H., Philo, D., Duong, A. T., Chang, K., Kako, T., Bahnemann, D. W., & Ye, J. (2019). Photogenerated charge carriers dynamics on La- and/or Cr-doped $SrTiO_3$ nanoparticles studied by transient absorption spectroscopy. *The Journal of Physical Chemistry C, 124*(2), 1292–1302.

Ikram, M., Shahzadi, A., Bilal, M., Haider, A., Ul-Hamid, A., Nabgan, W., Jaider, J., Ali, S. & Imran, M. (2023). Strontium-doped chromium oxide for RhB reduction and antibacterial activity with evidence of molecular docking analysis. *Frontiers in Chemistry, 11*, 1167701.

Iriani, Y., Afriani, R. , Sandi, D. K. , & Nurosyid, F. (2022). Co-precipitation synthesis and photocatalytic activity of Mn-doped $SrTiO_3$ for the degradation of methylene blue wastewater. *Evergreen, 9*(4), 1039–1045.

Iriani, Y., Afriani, R., Sandi, D. K., & Nurosyid, F. (2023). Photocatalysts comparison of low Mn-doped $SrTiO_3$ ($SrTi_{1-x}Mn_xO_3$; x=1% and 3%). *Materials Science Forum, 1111*, 129–134.

Iriani, Y., Sandi, D. K., Hikmah D. N., Afriani, R., Nurosyid, F., Handoko, E., & Faquelle, D. (2024a). Comparison study of aluminum (Al)-doped strontium titanate ($SrAl_xTi_{1-x}O_3$; x = 3 % and 5 %) photocatalyst for methylene blue degradation. *Materials Today: Proceedings,* https://doi:10.1016/j.matpr.2024.03.042.

Iriani, Y., Puspita, N. F. S., Sandi, D. K., Nurosyid, F., Suryana, R., & Fasquelle, D. (2024b). The improved photocatalytic performance of strontium titanate (STO) powder induced by lanthanum dopants. *Iranian Journal of Materials Science and Engineering,* 21(4), 3645.

Irshad, M., Ain, Q. T., Zaman, M., Aslam, M.Z., Kousar, N., Asim, M., Rafique, M., Siraj, K., Tabish, A. N., Usman, M., Farooq, M.H., Assiri, M. A., & Imran, M. (2022). Photocatalysis and perovskite oxide-based materials: a remedy for a clean and sustainable future. *RSC Advances, 12*(12), 7009–7039.

Jagadeeswararao, M., Galian, R. E., & Perez-Prieto, J. (2023). Photocatalysis based on metal halide perovskites for organic chemical transformations. *Nanomaterials (Basel), 14*(1), 94.

Jiang, D., Sun, X., Wu, X., Shi, L. & Du, F. (2020). Hydrothermal synthesis of single-crystal Cr-doped $SrTiO_3$ for efficient visible-light responsive photocatalytic hydrogen evolution. *Materials Research Express, 7*(1), 015047.

Kaiya, K., Ueki, Y., Kawamoto, H., Watanabe, K., Yoshino, S., Yamaguchi, Y., & Kudo, A. (2024). Water splitting over transition metal-doped $SrTiO_3$ photocatalysts with response to visible light up to 660 nm. *Chemical Science,* 15(39), 16025–16033.

Kafeshani, M. A., Mahdikhah, V., & Sheibani, S. (2022). Facile preparation and modification of SrTiO3 through Ni–Cd co-doping as an efficient visible-light-driven photocatalyst. *Optical Materials, 133*, 113080.

Khoudro, A., Diab, M., & Al-aboush, O. (2024). Effect of chromium doping on the structural properties of strontium fluoride compound. *Chemistry and Materials Research, 16*(1), 1–6.

Lestari, I. D., Iriani, Y., Suryana, R., Sandi, D. K. & Ardi, E. K. A. (2025). Effect of nickel and lanthanum co-doping on photocatalytic activity of strontium titanate. *Defect and Diffusion Forum, 438,* 3–10.

Lopez-Juarez, R. (2021). Microwave-hydrothermal synthesis and photocatalytic properties of Cr-doped $SrTiO_3$ powder. *Ceramics - Silikaty*, *65*(2), 113–119.

Miran, H. A., Jaf, M. A., Tarawneh, T., Rahman, M. M., Al-Bayati, A. T., & Salman, E. M. T. (2023). First-principles Analysis of Cr-doped $SrTiO_3$ perovskite as optoelectronic materials. *Iranian Journal of Materials Science and Engineering, 20*(1), 1–12.

Murthy, P. K., Kiran, K. S., & Melagiriyappa, E. (2024). Influence of Nd^{3+} on structural, electrical and magnetic properties of Ni-Cd nanoferrites. *Physics Open, 21*, 100240.

Nakamoto, T., Iguchi, S., Naniwa, S., Tanaka, T., & Teramura, K. (2023). Mg-doped $SrTiO_3$ photocatalyst with Ag–Co cocatalyst for enhanced selective conversion of CO_2 to CO using H_2O as the electron donor. *Catalysis Science & Technology, 13*(15), 4534–4541.

Namade, L. D., Band, S. S., Pawar, P. K., Patil, A. R., Pdeamekar, R. S., Managave, K. G., Ganbavle, V. V., & Rajpure, K. Y. (2025). Ultraviolet light-driven degradation of organic dyes using $SrTiO_3$ photocatalytic nanoparticles. *Colloids and Surfaces A: Physicochemical and Engineering Aspects, 708*, 135976.

Navalon, S., Dhakshinamoorthy, A., Alvaro, M., Ferrer, B., & Garcia, H. (2023). Metal-organic frameworks as photocatalysts for solar-driven overall water splitting. *Chemical Reviews,* 123(1), 445–490.

Nkwachukwu, O. V., & Arotiba, O. A. (2021). Perovskite oxide-based materials for photocatalytic and photoelectrocatalytic treatment of water. *Frontiers in Chemistry, 9*, 634630.

Nkwachukwu, O. V., Muzenda, C., Jayeola, K. D., Sebokolodi, T. I., Sipuka, D.S., Cretin, M., Zhou, M., Nkosi, D., & Arotiba, O. A. (2023). Photoelectrocatalytic degradation of methylene blue on electrodeposited bismuth ferrite perovskite films. *Materials (Basel), 16*(7), 2769

Okunaka, S., Nakamura, T., Ikeda, T., Tsuruda, K., & Tokudome, H. (2024). Solar-driven simultaneous production of hypochlorous acid and hydrogen from saline water over $RhCrO_x$-loaded $SrTiO_3$ photocatalyst systems. *Sustainable Energy & Fuels,* 8(4), 745–751.

Ordoñez, M. F., Falletta, E., Cerrato, G., & Bianchi, C. L. (2024). Visible light active Ag@$SrTiO_3$: A powerful photocatalyst for NOx degradation. *Journal of Photochemistry and Photobiology A: Chemistry, 456* 115805.

Qin, Y., Wan, Y., Xiang, L., Wang, T., Guo, D., Fang, D., & Chang, K. (2024). Micro-regulating defect-charge delocalization in Cr-doped $SrTiO_3$ for boosting visible-light-driven overall water splitting. *Journal of Catalysis, 437*, 115660.

Rastgar, S., Rezaei, H., Younesi, H., & Abyar, H. (2022). Low-cost magnetic char derived from oily sludge for Methylene blue dye removal: Optimization, isotherm, and kinetic approach, *Advances in Environmental Technology*, *8(*4), 329–343.

Rastgar, S., Rezaei, H., Younesi, H., & Abyar, H. (2024). Preparation of superparamagnetic AC/Fe_3O_4/TiO_2 nanoparticles from magnetic waste oily petroleum sludge (MWOPS): Comprehensive characterization, H_2 production, design batch photoreactor, and treatment of oily petroleum wastewater (OPW) under UVA light. *Carbon Letters, 34*(6), 1673–1691.

Rastgar, S., Rezaei, H., Younesi, H., Abyar, H., & Kordrostami, A. (2023). Photocatalytic degradation of methylene blue (MB) dye under UV light irradiation by magnetic diesel tank sludge (MDTS).

Biomass Conversion and Biorefinery, *14*(17), 20451–20462.

Rastgar, S., Younesi, H., Rezeai, H., & Abyar, H. (2025). Innovative treatment of toxic oily petroleum wastewater with magnetic sludge under UVA light. *Petroleum Research,* 10(2), 383–403.

Sandi, D. K., Andini, T., Nurosyid, F., & Iriani, Y. (2025). Influence of high Sr^{2+} substitution on the structure and photocatalytic activity of $Ba_{1-X}Sr_XTiO_3$ for dye degradation. *Indonesian Journal of Applied Physics, 15*(2), 382–392.

Sharma, D. K., Sain, S., Maity, G., Thomas, A., Kumar, R., Dhar, S., Arora, H. S., Babu, B., & Roy, S. S. (2024). Electrochemical studies on chromium doped $SrTiO_3$ for supercapacitor applications. *Nano Trends*, *6*, 100036

Stajcic, I., Serpa, C., Simovi, B., Castvan, I. J., Dodevski, V., Radojevic, V., & Stajcic, A. (2024). Fractal analysis of doped strontium yitanate photocatalyst. *Fractal and Fractional, 8*(10), 560.

Talanov, M. V., Stash, A. I., Ivanov, S. A., Zhukova, E.S., Gorshunov, B. P., Nekrasov, B. M., Melentev, A. V., Kozlov, V. I., Cherepanoc, V.M., Gavrikin, S. Y., Yu, Tsvetkov, A. Y., Zavidovskiy, I. A., Tatmyshevskiy, M. K., Savinov, M., Talanov, V. M., & Bush, A. A. (2024). Transition metal-doped $SrTiO_3$: when does a tiny chemical impact have such a great structural response?. *Journal of Materials Chemistry C, 12*(22), 8105–8118.

Tenzin, T., Yashas, S. R., Anilkumar, K. M., & Shivaraju, H. P. (2021). UV–LED driven photodegradation of organic dye and antibiotic using strontium titanate nanostructures. *Journal of Materials Science: Materials in Electronics, 32*(16), 21093–21105.

Tsaviv, J. N., Eneji, I. S., Shato'Ato, R., Ahemen, I., Jubu, P. R., & Yusof, Y. (2024). Photocatalytic studies of methylene blue dye degradation on synthesized Ni-doped strontium zirconate perovskite nanoparticles. *ChemSearch Journal*, *15*(1), 219–237.

Wang, D., Ye, J., Kako, T., & Kimura, T. (2006). Photophysical and photocatalytic properties of $SrTiO_3$ doped with Cr cations on different sites. *The Journal of Physical Chemistry B, 110*(32), 15824–15830.

Xu, R., Xiang, L., Zhu, X., Ding, L., Fang, F., & Chang, K. (2025). Structure-balance-responsive V^{4+} ions in $SrTiO_3$ crystal for efficient visible-light-driven overall water splitting. *Ceramics International, 51*(6), 7193–7201.

Zamani, W., Rastgar, S., Hedayati, A. (2023a). Capability of $TiO_{(2)}$ and $Fe_{(3)}O_{(4)}$ nanoparticles loaded onto Algae (Scendesmus sp.) as a novel bio-magnetic photocatalyst to degration of Red195 dye in the sonophotocatalytic treatment process under ultrasonic/ UVA irradiation. *Scientific Reports, 13*(1), 18182.

Zamani, W., Rastgar, S., & Hedayati, A. (2023b) Using oyster shell (Andonata Cygnea) as a novel biophotocatalyst for fish farm wastewater treatment with response surface methodology (RSM): Isotherm, kinetics, and thermodinamics. *Biomass Conversion and Biorefinery,* 14(24), 31217–31232.